Computational Mechanics manuscript No.
(will be inserted by the editor)

On special CFD techniques for the efficient solution of dynamic porous media problems

S. Turek · A. Obaid · B. Markert

Received: date / Accepted: date

Abstract We present an efficient monolithic finite element solution scheme to solve the set of PDEs governing a two-dimensional biphasic saturated TPM model with intrinsically coupled solid and fluid constituents. Our approach, coming from CFD techniques and originally developed for the efficient simulation of incompressible flow problems, is characterized by the following aspects: (1) a special treatment of the coupled volume balance equation leading to a reduced form of the boundary conditions; (2) the considered fluid viscosity for enhancing the stability of the algorithm; (3) the usage of a higher order accurate mixed finite element pair for the spatial discretization of the equations; (4) the adoption of the fully implicit 2nd order Crank-Nicolson scheme for the time discretization; (5) a special fast multigrid solver to solve the resulting discrete linear systems. For the purpose of validation and to expose the merits and benefits of our new solution method compared to other established ones, canonical one- and two-dimensional wave propagation examples were opted while a large scale problem was chosen from the literature to test the efficiency of the special multigrid solver in combination with our FEM discretization.

Keywords Multigrid solver · Porous media dynamics · Coupled problem · Monolithic solution · Fully implicit · Finite element method · CFD

1 Theoretical fundamentals

In preparation of the numerical treatment, the governing equations of porous media dynamics are briefly recapitulated. This includes the porous media modeling approach, the corresponding kinematics as well as the equilibrium and constitutive relations. For a more detailed discussion, the interested reader is referred to [3, 5, 13] and the citations therein.

1.1 Macroscopic porous media approach

In the framework of the Theory of Porous Media (TPM) [7], we proceed from a continuum-mechanical description of a fluid-filled porous body consisting of a solid matrix saturated by a single pore fluid.

S. Turek · A. Obaid
Dortmund University of Technology, Institute of Applied Mathematics (LS3)
Vogelpothsweg 87, 44227 Dortmund, Germany
Tel.: +49-231-755-3075
Fax: +49-231-755-5933
E-mail: {stefan.turek,aobaid}@math.tu-dortmund.de

B. Markert
University of Stuttgart, Institute of Applied Mechanics (CE)
Pfaffenwaldring 7, 70569 Stuttgart, Germany
Tel.: +49-711-685-66346
Fax: +49-711-685-66347
E-mail: bernd.markert@mechbau.uni-stuttgart.de

Thereby, the binary aggregate is treated as a macroscopic mixture φ with overlaid and interacting but de facto immiscible solid and fluid constituents φ^α ($\alpha = S$: solid; $\alpha = F$: fluid), so that $\varphi = \varphi^S \cup \varphi^F$ at any macroscopic spatial point $\mathbf{x}(t)$ at any time $t \in [t_0, T]$. The local composition of the biphasic continuum is described by volume fractions $n^\alpha(\mathbf{x}, t) := \mathrm{d}v^\alpha / \mathrm{d}v \in (0, 1)$ of φ^α (n^S : solidity; n^F : porosity) defined as the ratios of the partial to the total volume elements of φ. Assuming fully saturated conditions, the saturation constraint obviously yields $\sum_\alpha n^\alpha = n^S + n^F = 1$. Closely related is the introduction of two density functions, namely an effective density $\rho^{\alpha R}(\mathbf{x}, t)$ and a partial density $\rho^\alpha(\mathbf{x}, t)$ relating the local mass of φ^α to the partial or the bulk volume element, respectively. It is easily seen that $\rho^\alpha = n^\alpha \rho^{\alpha R}$ revealing the general compressibility of porous solids through possible changes of the pore space.

Following the kinematics of mixtures, the superimposed continuum formulation proceeds from unique individual states of motion with each constituent having its own velocity and acceleration field

$$\mathbf{v}_\alpha := \overset{\prime}{\mathbf{x}}_\alpha \,, \quad (\mathbf{v}_\alpha)'_\alpha = \overset{\prime\prime}{\mathbf{x}}_\alpha \quad \text{with} \quad (\bullet)'_\alpha := \frac{\mathrm{d}_\alpha(\bullet)}{\mathrm{d}t} = \frac{\partial(\bullet)}{\partial t} + \operatorname{grad}(\bullet) \cdot \mathbf{v}_\alpha \tag{1}$$

as the material time derivative following the motion of φ^α and $\operatorname{grad}(\bullet) = \dfrac{\partial(\bullet)}{\partial \mathbf{x}}$. In porous media theories, it is convenient to proceed from a Lagrangian description of the solid matrix via the solid displacement $\mathbf{u}_S$ and velocity $\mathbf{v}_S$ as the kinematical variables. However, the pore-fluid flow is expressed either in a modified Eulerian setting via the seepage velocity vector $\mathbf{w}_{FS}$ describing the fluid motion relative to the deforming skeleton, or by an Eulerian description using the fluid velocity $\mathbf{v}_F$ itself. In particular, we have

$$\mathbf{u}_S = \mathbf{x} - \mathbf{X}_S \,, \quad \mathbf{v}_S = (\mathbf{u}_S)'_S = \overset{\prime}{\mathbf{x}}_S \,, \quad \mathbf{v}_F = \overset{\prime}{\mathbf{x}}_F \,, \quad \mathbf{w}_{FS} = \mathbf{v}_F - \mathbf{v}_S \,. \tag{2}$$

1.2 Equilibrium and constitutive relations

The considered biphasic model excludes thermal effects as well as any mass exchanges (inert φ^α) and proceeds from intrinsically incompressible constituents ($\rho^{\alpha R} = \text{const.}$). In particular, the arising purely mechanical, binary model with $\alpha = \{S, F\}$ is governed by the following constituent balance equations:

- Partial mass balance $\longrightarrow$ partial volume balance:

$$(\rho^\alpha)'_\alpha + \rho^\alpha \operatorname{div} \mathbf{v}_\alpha = 0 \qquad \longrightarrow \quad (n^\alpha)'_\alpha + n^\alpha \operatorname{div} \mathbf{v}_\alpha = 0 \tag{3}$$

- Partial momentum balance:

$$\rho^\alpha (\mathbf{v}_\alpha)'_\alpha = \operatorname{div} \mathbf{T}^\alpha + \rho^\alpha \, \mathbf{b} + \hat{\mathbf{p}}^\alpha \tag{4}$$

Here, $\operatorname{div}(\bullet)$ is the divergence operator related to $\operatorname{grad}(\bullet)$, $\mathbf{T}^\alpha = (\mathbf{T}^\alpha)^T$ is the symmetric partial Cauchy stress assuming non-polar constituents, $\mathbf{b}$ is the mass-specific body force acting on the overall aggregate, and $\hat{\mathbf{p}}^\alpha$ denotes the direct momentum production, which can be interpreted as the volume-specific local interaction force between the percolating pore fluid and the solid skeleton. Due to the overall conservation of momentum, $\hat{\mathbf{p}}^S + \hat{\mathbf{p}}^F = \mathbf{0}$ must hold for any closed multiphasic system. From (3) with $\alpha = S$ and $(n^S \rho^{SR})'_S = (n^S)'_S \, \rho^{SR}$, one directly obtains the solidity as a secondary variable by integration

$$(n^S)'_S = -n^S \operatorname{div} \mathbf{v}_S \quad \longrightarrow \quad n^S = n^S_{0S} \det \mathbf{F}_S^{-1} \tag{5}$$

with n^S_{0S} being the initial volume fraction of φ^S at time t_0 and $\mathbf{F}_S = \partial \mathbf{x} / \partial \mathbf{X}_S$ as the solid deformation gradient. Proceeding from a small strain approach, n^S can be written in geometrically linear form as

$$n^S \approx n^S_{0S} \, (1 - \operatorname{div} \mathbf{u}_S) \,. \tag{6}$$

To continue, according to the principle of effective stresses, see [1] for references, $\mathbf{T}^\alpha$ and $\hat{\mathbf{p}}^F$ can be split into effective field quantities, the so-called extra terms indicated by the subscript $(\bullet)_E$, and parts that are governed by the pore-fluid pressure p

$$\mathbf{T}^\alpha = \mathbf{T}^\alpha_E - n^\alpha p \, \mathbf{I} \,, \quad \hat{\mathbf{p}}^F = \hat{\mathbf{p}}^F_E + p \operatorname{grad} n^F \tag{7}$$

with $\mathbf{I}$ being the 2nd-order identity tensor. With regard to a thermodynamically consistent model, admissible constitutive equations for the response functions $\mathbf{T}_E^\alpha$ and $\hat{\mathbf{p}}_E^F$ must be provided. Restricting the presentation to the small strain regime, the solid extra stress is determined by the Hookean elasticity law

$$\mathbf{T}_E^S = 2\mu^S\,\boldsymbol{\varepsilon}_S + \lambda^S\,(\boldsymbol{\varepsilon}_S \cdot \mathbf{I})\,\mathbf{I} \qquad \text{with} \qquad \boldsymbol{\varepsilon}_S = \tfrac{1}{2}\,(\operatorname{grad}\mathbf{u}_S + \operatorname{grad}^T\mathbf{u}_S) \tag{8}$$

as the geometrically linear solid strain tensor and μ^S, λ^S being the macroscopic Lamé constants of the porous solid matrix. Furthermore, under the assumption of isotropic lingering flow conditions at low Reynolds numbers, the percolation process is appropriately described by a linear Darcy-type filter law, which can be traced back to the simple but thermodynamically consistent ansatz

$$\hat{\mathbf{p}}_E^F = -\frac{(n^F)^2\,\gamma^{FR}}{k^F}\,\mathbf{w}_{FS} \tag{9}$$

where $k^F > 0$ denotes the conventional hydraulic conductivity (Darcy permeability) in m/s and $\gamma^{FR} = \rho^{FR} g$ is the effective fluid weight with $g = |\mathbf{b}| = \text{const.}$ as the scalar gravitational acceleration. Moreover, using (1), the material time derivative with respect to the fluid motion can be written as:

$$(\,\bullet\,)'_F = (\,\bullet\,)'_S + \operatorname{grad}(\,\bullet\,)\cdot\mathbf{w}_{FS} \tag{10}$$

In summary, inserting the aforementioned constitutive and kinematic relations into (4), the governing set of partial differential equations (PDE) reads:

- Solid Balance of Momentum

$$\rho^S(\mathbf{v}_S)'_S = \operatorname{div}\mathbf{T}_E^S - n^S\operatorname{grad}p + \rho^S\mathbf{b} + \frac{(n^F)^2\,\gamma^{FR}}{k^F}\,(\mathbf{v}_F - \mathbf{v}_S) \tag{11}$$

- Fluid Balance of Momentum

$$\begin{aligned}\rho^F(\mathbf{v}_F)'_S = \operatorname{div}\mathbf{T}_E^F - n^F\operatorname{grad}p + \rho^F\,\mathbf{b} - \frac{(n^F)^2\,\gamma^{FR}}{k^F}\,(\mathbf{v}_F - \mathbf{v}_S)\\ -\rho^F(\operatorname{grad}\mathbf{v}_F)(\mathbf{v}_F - \mathbf{v}_S)\end{aligned} \tag{12}$$

- Volume balance of the overall aggregate

$$\operatorname{div}(n^F\mathbf{v}_F) + \operatorname{div}(n^S\mathbf{v}_S) = 0 \tag{13}$$

Note that the chosen primary unknowns for this set of PDE are $\mathbf{u}_S$, $\mathbf{v}_F$ and p. Hence, $\mathbf{v}_S(\mathbf{u}_S)$ as well as $\mathbf{T}_E^S(\mathbf{u}_S)$, $\mathbf{T}_E^F(\mathbf{v}_F)$, $n^S(\mathbf{u}_S)$, $n^F(\mathbf{u}_S)$ and $\mathbf{w}_{FS}$ represent the secondary variables of the problem. Additionally, a reduction in the order of the PDE to order-one in time is achieved using

$$(\mathbf{u}_S)'_S = \mathbf{v}_S \tag{14}$$

which eliminates the second time derivative of the solid displacement from (11), and allows the applicability of a wide range of fundamental time-stepping algorithms.

1.3 Reduction of the complete set of model equations

For the purpose of simplification, several terms in equations (11)-(13) have been canceled, which are marked with blue and red color in the following description:

$$\rho^S(\mathbf{v}_S)'_S = \operatorname{div}\mathbf{T}_E^S - n^S\operatorname{grad}p + \rho^S\mathbf{b} + \frac{(n^F)^2\,\gamma^{FR}}{k^F}\,(\mathbf{v}_F - \mathbf{v}_S) \tag{15}$$

$$\begin{aligned}\rho^F(\mathbf{v}_F)'_S + \rho^F(\operatorname{grad}\mathbf{v}_F)(\mathbf{v}_F - \mathbf{v}_S) \approx 0 = \operatorname{div}\mathbf{T}_E^F - n^F\operatorname{grad}p + \rho^F\,\mathbf{b}\\ -\frac{(n^F)^2\,\gamma^{FR}}{k^F}\,(\mathbf{v}_F - \mathbf{v}_S)\end{aligned} \tag{16}$$

$$\underbrace{\operatorname{grad} n^F}_{\approx 0} \cdot \mathbf{v}_F + \underbrace{\operatorname{grad} n^S}_{\approx 0} \cdot \mathbf{v}_S + n^F \operatorname{div} \mathbf{v}_F + n^S \operatorname{div} \mathbf{v}_S = 0 \tag{17}$$

Here, n^S and n^F are assumed to be constant, which is acceptable for the small deformation case, such that the blue terms are dropped out. Furthermore, proceeding from a geometrically linear description, the (red) nonlinear convective term can be omitted by scaling arguments if $\operatorname{grad}(\bullet) \cdot \mathbf{w}_{FS} \ll (\bullet)'_S$ yielding $(\bullet)'_F \approx (\bullet)'_S$. To continue with linear PDEs, the pore fluid is assumed to be Newtonian and incompressible leading to the following relation:

$$\operatorname{div} \mathbf{T}_E^F = \nu \Delta \mathbf{v}_F \tag{18}$$

However, in spite of its negligible influence (cf. [12]), this term containing the (small) fluid viscosity is nevertheless considered in our subsequent discretization and solution approaches, which will be explained in the following sections.

2 Weak formulation and discretization in space and time

Our subsequent variational form of the **uvp** approach, which is inspired by weak formulations that are typical in the CFD community for treating the incompressible Navier-Stokes equations, is created by multiplying (15)-(17) with the displacement test function $\delta \mathbf{u}_S$, the velocity test function $\delta \mathbf{v}_F$, the pressure test function δp, integrating over the whole domain Ω and performing partial integrations. Finally, we obtain the following weak form which is similar to the standard one for porous media (see, for instance, page 1349 of [13]):

$$\begin{aligned} &\int_\Omega \operatorname{grad} \delta \mathbf{u}_S : \mathbf{T}_E^S \, \mathrm{d}v - \int_\Omega \frac{(n^F)^2 \gamma^{FR}}{k^F} \delta \mathbf{u}_S \cdot \mathbf{v}_F \, \mathrm{d}v - \int_\Omega n^S \operatorname{div} \delta \mathbf{u}_S \; p \, \mathrm{d}v + \\ &\int_\Omega \frac{(n^F)^2 \gamma^{FR}}{k^F} \delta \mathbf{u}_S \cdot \mathbf{v}_S \, \mathrm{d}v + \int_\Omega \rho^S \delta \mathbf{u}_S \cdot \left\{ (\mathbf{v}_S)'_S - \mathbf{b} \right\} \mathrm{d}v = \int_{\Gamma_{\mathbf{t}^S}} \delta \mathbf{u}_S \cdot \bar{\mathbf{t}}^S \, \mathrm{d}a \end{aligned} \tag{19}$$

$$\begin{aligned} &\int_\Omega \nu \operatorname{grad} \delta \mathbf{v}_F : \operatorname{grad} \mathbf{v}_F \, \mathrm{d}v + \int_\Omega \frac{(n^F)^2 \gamma^{FR}}{k^F} \delta \mathbf{v}_F \cdot \mathbf{v}_F \, \mathrm{d}v - \int_\Omega n^F \operatorname{div} \delta \mathbf{v}_F \; p \, \mathrm{d}v - \\ &\int_\Omega \frac{(n^F)^2 \gamma^{FR}}{k^F} \delta \mathbf{v}_F \cdot \mathbf{v}_S \, \mathrm{d}v + \int_\Omega \rho^F \delta \mathbf{v}_F \cdot \left\{ (\mathbf{v}_F)'_S - \mathbf{b} \right\} \mathrm{d}v = \int_{\Gamma_{\mathbf{t}^F}} \delta \mathbf{v}_F \cdot \bar{\mathbf{t}}^F \, \mathrm{d}a \end{aligned} \tag{20}$$

$$\int_\Omega n^S \delta p \; \operatorname{div} \mathbf{v}_S \, \mathrm{d}v + \int_\Omega n^F \delta p \; \operatorname{div} \mathbf{v}_F \, \mathrm{d}v = 0 \tag{21}$$

Here, the red-colored terms represent slight differences to [13], namely the additional fluid viscosity term and the natural shape of the weak form of the volume balance. Finally, we multiply (14) with $\delta \mathbf{u}_S$ and integrate over Ω:

$$\int_\Omega \delta \mathbf{u}_S \cdot \left\{ (\mathbf{u}_S)'_S - \mathbf{v}_S \right\} \mathrm{d}v = 0 \tag{22}$$

The boundary $\Gamma = \partial \Omega$ is divided into Dirichlet (essential) and Neumann (natural) boundaries, respectively, resulting in $\Gamma = \Gamma_{\mathbf{u}_S} \cup \Gamma_{\mathbf{t}^S}$ for the solid momentum balance and in $\Gamma = \Gamma_{\mathbf{v}_F} \cup \Gamma_{\mathbf{t}^F}$ for the fluid momentum balance, wherein the tractions are defined as:

$$\mathbf{t}^S = \left(\mathbf{T}_E^S - n^S p \mathbf{I} \right) \cdot \mathbf{n}, \qquad \mathbf{t}^F = \nu \frac{\partial \mathbf{v}_F}{\partial \mathbf{n}} - n^F p \mathbf{n} \tag{23}$$

Keep in mind that due to the fact that the pressure (as Lagrange multiplier regarding the incompressibility constraint) provides typically less regularity than displacement and velocity, the pressure derivatives in the weak formulation have been eliminated by partial integration. For the same reason and as usual for the treatment of the incompressible Navier-Stokes equations, no integration by parts has been carried out in (21).

Using such a weak form, which avoids derivatives acting on the pressure functions, one can use standard FEM pairs for velocity/displacement and pressure as typical for incompressible flow problems,

which are based on piecewise discontinuous pressure approximations (as shown in Figure 1), and the boundary conditions are imposed in a modified way allowing for a wide range of problems to be solved. As a candidate for LBB-stable Stokes elements, we apply in the following (2D) simulations the well-known (non-parametric) Q2/P1 element, that means biquadratic velocities and displacements and piecewise linear (discontinuous) pressure approximations (cf. [17]), which belongs currently to the 'best' FEM choices for incompressible flow problems in regard to efficiency, accuracy and robustness.

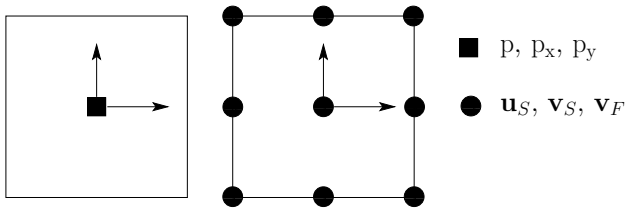

Fig. 1 The discontinuous linear pressure element P1 (left) and the 9-node Lagrange biquadratic element Q2 (right) that we use for our **uv***p*(3)-TR method.

Since we want to show explicit comparisons with a more classical (here: **uv***p*-TB2) approach (see [13]), we additionally introduce the Taylor-Hood-like element in Figure 2, with biquadratic (Q) approximations for some degree of freedoms omitting the internal node (serendipity element), and continuous bilinear (L) approximations for other degree of freedoms.

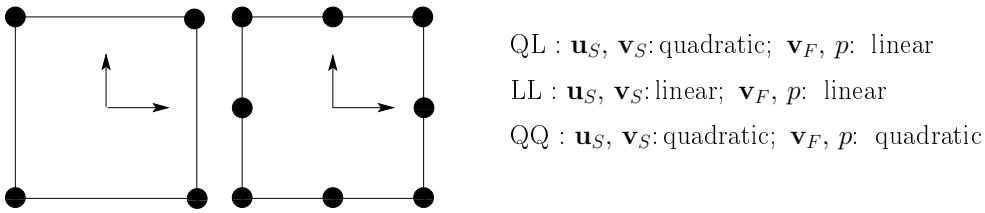

Fig. 2 The standard 4-node bilinear element L (left) and the 8-node serendipity quadrilateral element Q (right) that is used for the uvp-TB2 method.

Next, based on the discretization with the introduced FEM spaces, equations (19)-(22) can be written in the following matrix-vector notation

$$\mathbf{M}\dot{\mathbf{y}} + \mathbf{K}\mathbf{y} = \mathbf{f}\,. \tag{24}$$

In more detail with mass and stiffness matrices and right hand side vectors, one obtains

$$\underbrace{\begin{pmatrix} \mathbf{0} & \mathbf{M}_{\mathbf{u}_S\mathbf{v}_S} & \mathbf{0} & \mathbf{0} \\ \mathbf{M}_{\mathbf{v}_S\mathbf{u}_S} & \mathbf{0} & \mathbf{0} & \mathbf{0} \\ \mathbf{0} & \mathbf{0} & \mathbf{M}_{\mathbf{v}_F\mathbf{v}_F} & \mathbf{0} \\ \mathbf{0} & \mathbf{0} & \mathbf{0} & \mathbf{0} \end{pmatrix}}_{\mathbf{M}} \underbrace{\begin{pmatrix} \dot{\mathbf{u}}_S \\ \dot{\mathbf{v}}_S \\ \dot{\mathbf{v}}_F \\ \dot{p} \end{pmatrix}}_{\dot{\mathbf{y}}} + \underbrace{\begin{pmatrix} \mathbf{K}_{\mathbf{u}_S\mathbf{u}_S} & \mathbf{K}_{\mathbf{u}_S\mathbf{v}_S} & \mathbf{K}_{\mathbf{u}_S\mathbf{v}_F} & \mathbf{K}_{\mathbf{u}_S p} \\ \mathbf{0} & \mathbf{K}_{\mathbf{v}_S\mathbf{v}_S} & \mathbf{0} & \mathbf{0} \\ \mathbf{0} & \mathbf{K}_{\mathbf{v}_F\mathbf{v}_S} & \mathbf{K}_{\mathbf{v}_F\mathbf{v}_F} & \mathbf{K}_{\mathbf{v}_F p} \\ \mathbf{0} & \mathbf{K}_{p\mathbf{v}_S} & \mathbf{K}_{p\mathbf{v}_F} & \mathbf{0} \end{pmatrix}}_{\mathbf{K}} \underbrace{\begin{pmatrix} \mathbf{u}_S \\ \mathbf{v}_S \\ \mathbf{v}_F \\ p \end{pmatrix}}_{\mathbf{y}} = \underbrace{\begin{pmatrix} \mathbf{f}_{\mathbf{u}_S} + \mathbf{b}_S \\ \mathbf{0} \\ \mathbf{f}_{\mathbf{v}_F} + \mathbf{b}_F \\ \mathbf{0} \end{pmatrix}}_{\mathbf{f}} \tag{25}$$

with the following matrices and right hand side vectors:

$$
\begin{aligned}
&\mathbf{K}_{\mathbf{u}_S\mathbf{u}_S} = \int_\Omega \operatorname{grad}\delta\mathbf{u}_S : \mathbf{T}_E^S \,\mathrm{d}v\,, \quad \mathbf{K}_{\mathbf{u}_S\mathbf{v}_S} = \int_\Omega \frac{(n^F)^2\,\gamma^{FR}}{k^F}\,\delta\mathbf{u}_S\cdot\mathbf{v}_S\,\mathrm{d}v\\
&\mathbf{K}_{\mathbf{u}_S\mathbf{v}_F} = -\int_\Omega \frac{(n^F)^2\,\gamma^{FR}}{k^F}\,\delta\mathbf{u}_S\cdot\mathbf{v}_F\,\mathrm{d}v\,, \quad \mathbf{K}_{\mathbf{u}_S p} = -\int_\Omega n^S \operatorname{div}\delta\mathbf{u}_S\; p\,\mathrm{d}v\\
&\mathbf{K}_{\mathbf{v}_S\mathbf{v}_S} = -\int_\Omega \delta\mathbf{u}_S\cdot\mathbf{v}_S\,\mathrm{d}v\,, \quad \mathbf{K}_{\mathbf{v}_F\mathbf{v}_S} = -\int_\Omega \frac{(n^F)^2\,\gamma^{FR}}{k^F}\,\delta\mathbf{v}_F\cdot\mathbf{v}_S\,\mathrm{d}v\\
&\mathbf{K}_{\mathbf{v}_F\mathbf{v}_F} = \int_\Omega \nu\operatorname{grad}\delta\mathbf{v}_F : \operatorname{grad}\mathbf{v}_F\,\mathrm{d}v + \int_\Omega \frac{(n^F)^2\,\gamma^{FR}}{k^F}\,\delta\mathbf{v}_F\cdot\mathbf{v}_F\,\mathrm{d}v\\
&\mathbf{K}_{\mathbf{v}_F p} = -\int_\Omega n^F \operatorname{div}\delta\mathbf{v}_F\; p\,\mathrm{d}v\,, \quad \mathbf{K}_{p\mathbf{v}_S} = \int_\Omega n^S\delta p\;\operatorname{div}\mathbf{v}_S\,\mathrm{d}v\\
&\mathbf{K}_{p\mathbf{v}_F} = \int_\Omega n^F\delta p\;\operatorname{div}\mathbf{v}_F\,\mathrm{d}v\,, \quad \mathbf{M}_{\mathbf{u}_S\mathbf{v}_S} = \int_\Omega \left\{n^S\rho^{SR}\right\}\delta\mathbf{u}_S\cdot(\mathbf{v}_S)'_S\,\mathrm{d}v\\
&\mathbf{M}_{\mathbf{v}_S\mathbf{u}_S} = \int_\Omega \delta\mathbf{u}_S\cdot(\mathbf{u}_S)'_S\,\mathrm{d}v\,, \quad \mathbf{M}_{\mathbf{v}_F\mathbf{v}_F} = \int_\Omega \left\{n^F\rho^{FR}\right\}\delta\mathbf{v}_F\cdot(\mathbf{v}_F)'_S\,\mathrm{d}v\\
&\mathbf{f}_{\mathbf{u}_S} = \int_{\Gamma_{\mathbf{t}S}} \delta\mathbf{u}_S\cdot\bar{\mathbf{t}}^S\,\mathrm{d}a\,, \quad \mathbf{f}_{\mathbf{v}_F} = \int_{\Gamma_{\mathbf{t}F}} \delta\mathbf{v}_F\cdot\bar{\mathbf{t}}^F\,\mathrm{d}a\\
&\mathbf{b}_S = \int_\Omega \left\{n^S\rho^{SR}\right\}\delta\mathbf{u}_S\cdot\mathbf{b}\,\mathrm{d}v\,, \quad \mathbf{b}_F = \int_\Omega \left\{n^F\rho^{FR}\right\}\delta\mathbf{v}_F\cdot\mathbf{b}\,\mathrm{d}v
\end{aligned}
\tag{26}
$$

In the next step, regarding the time integration, equations (25) or (24) are treated in a monolithic implicit way leading to a fully coupled system. In our approach, we apply the standard θ-scheme to these systems, which leads to

$$
\mathbf{M}\frac{\mathbf{y}_{n+1}-\mathbf{y}_n}{\Delta t} + \theta\mathbf{K}\mathbf{y}_{n+1} = -(1-\theta)\,\mathbf{K}\mathbf{y}_n + \theta\mathbf{f}_{n+1} + (1-\theta)\mathbf{f}_n\,. \tag{27}
$$

In the subsequent more detailed description, the blue-colored continuity equation and the red-colored pressure p as corresponding Lagrange multiplier are treated fully implicitly ($\theta = 1$) (cf. [17]). Finally, the time step Δt in front of the red terms is absorbed into $\bar{p} = \Delta t\, p$:

$$
\begin{pmatrix}
\Delta t\theta\mathbf{K}_{\mathbf{u}_S\mathbf{u}_S} & \mathbf{M}_{\mathbf{u}_S\mathbf{v}_S} + \theta\Delta t\mathbf{K}_{\mathbf{u}_S\mathbf{v}_S} & \theta\Delta t\mathbf{K}_{\mathbf{u}_S\mathbf{v}_F} & \mathbf{K}_{\mathbf{u}_S p}\\
\mathbf{M}_{\mathbf{v}_S\mathbf{u}_S} & \theta\Delta t\mathbf{K}_{\mathbf{v}_S\mathbf{v}_S} & 0 & 0\\
0 & \theta\Delta t\mathbf{K}_{\mathbf{v}_F\mathbf{v}_S} & \mathbf{M}_{\mathbf{v}_F\mathbf{v}_F} + \theta\Delta t\mathbf{K}_{\mathbf{v}_F\mathbf{v}_F} & \mathbf{K}_{\mathbf{v}_F p}\\
0 & \mathbf{K}_{p\mathbf{v}_S} & \mathbf{K}_{p\mathbf{v}_F} & 0
\end{pmatrix}
\begin{pmatrix}\mathbf{u}_S\\ \mathbf{v}_S\\ \mathbf{v}_F\\ \bar{p}\end{pmatrix}_{n+1}
=
$$

$$
\begin{pmatrix}
(\theta-1)\Delta t\mathbf{K}_{\mathbf{u}_S\mathbf{u}_S} & \mathbf{M}_{\mathbf{u}_S\mathbf{v}_S} + (\theta-1)\Delta t\mathbf{K}_{\mathbf{u}_S\mathbf{v}_S} & (\theta-1)\Delta t\mathbf{K}_{\mathbf{u}_S\mathbf{v}_F} & 0\\
\mathbf{M}_{\mathbf{v}_S\mathbf{u}_S} & (\theta-1)\Delta t\mathbf{K}_{\mathbf{v}_S\mathbf{v}_S} & 0 & 0\\
0 & (\theta-1)\Delta t\mathbf{K}_{\mathbf{v}_F\mathbf{v}_S} & \mathbf{M}_{\mathbf{v}_F\mathbf{v}_F} + (\theta-1)\Delta t\mathbf{K}_{\mathbf{v}_F\mathbf{v}_F} & 0\\
0 & 0 & 0 & 0
\end{pmatrix}
\begin{pmatrix}\mathbf{u}_S\\ \mathbf{v}_S\\ \mathbf{v}_F\\ \bar{p}\end{pmatrix}_{n}
+ \theta\Delta t\mathbf{f}_{n+1} + (1-\theta)\Delta t\mathbf{f}_n
\tag{28}
$$

After solving the above saddle-point systems, the pressure is scaled back using the relation $p = \bar{p}/\Delta t$. Setting $\theta = \frac{1}{2}$, we recover the second-order Crank-Nicolson scheme (in time), which is based on the well-known trapezoidal rule (TR). However, also fully L-stable 2nd order schemes like BDF(2) or Fractional-Step-Theta-schemes can be used in an analogous way.

3 Numerical validation

To validate and to evaluate our discussed formulations (which all have been realized in our in-house code FEATFLOW[1]), two numerical examples taken from [13] are introduced and implemented in order to compare with well-established methods. Our **uv**p(3)-TR-Q2/P1 approach stands for the described monolithic solver for the **uv**p formulation based on the weak forms (19)-(22) using the fully implicit Crank-Nicolson ($\theta = \frac{1}{2}$) time integration scheme as shown in (28) and the mixed finite element pairs Q2/P1 shown in Figure 1. The number 3 in **uv**p(3)-TR-Q2/P1 is used to distinguish our solution algorithms from those in Table I in [13]. Typically, we will show results for a sequence of consecutively refined meshes which are constructed by connecting opposite midpoints of the corresponding coarser meshes, starting from a basic mesh on mesh level 1.

Results I: Saturated poroelastic column under harmonic load

In this example, the response of a homogeneous and isotropic, water-saturated, poroelastic column (height: 10 m, width: 2 m) is analyzed under plane-strain, confined compression conditions. Therefore, the mixture domain is surrounded by impermeable, frictionless but rigid boundaries except for the loaded top side which is perfectly drained ($\mathbf{t}^F = \mathbf{0}$). The geometry with boundary conditions and the loading path are illustrated in Figure 3.

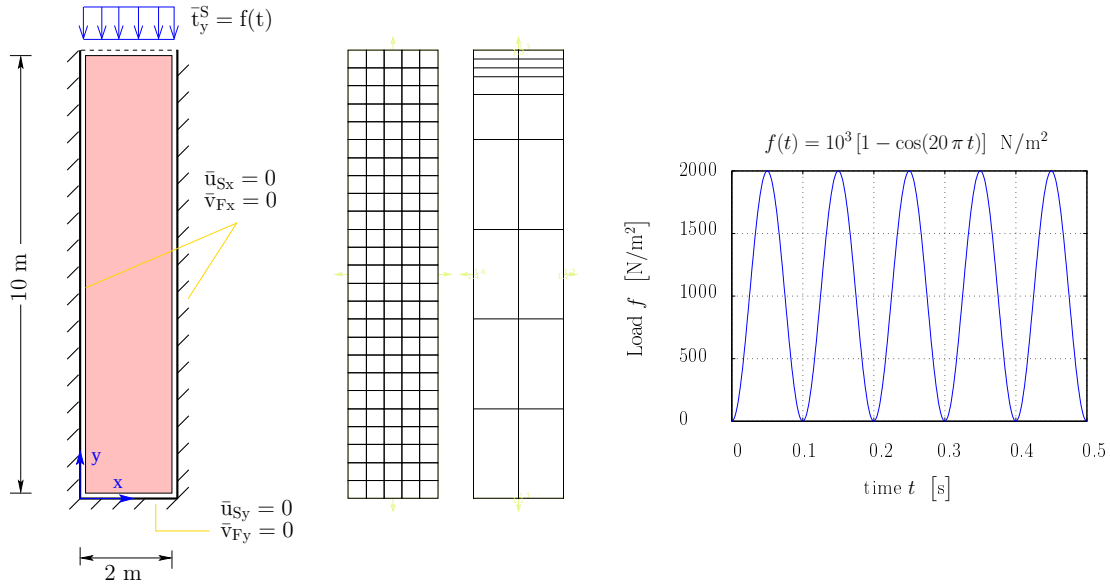

Fig. 3 Geometry, boundary conditions (left), FE meshes (mesh level 1, isotropic cartesian center-left and rectilinear center-right) and loading path (right) of the dynamic confined compression of a saturated poroelastic column. Non prescribed DOFs are automatically taken as natural boundary conditions.

Table 1 Total number of elements and unknowns (five primary unknowns u_{Sx}, u_{Sy}, v_{Fx}, v_{Fy} and p plus two secondary unknowns v_{Sx} and v_{Sy}) for the **uv**p(3)-TR-Q2/P1 approach. This table is related to Figure 3.

mesh level	cartesian		rectilinear	
	#Elements	#Unknowns	#Elements	#Unknowns
1	125: (5 elements per 2 m)	3 741	18	625
2	500: (5 elements per 1 m)	14 226	72	2 214
3	2000: (10 elements per 1 m)	55 446	288	8 310
4			1152	32 166
5			4608	126 534

[1] http://www.featflow.de

The constitutive material parameters are adopted from related literature [2] and listed in Table 2.

Table 2 Physical properties of the porous medium used for all simulations.

Parameter	Symbol	Value	SI unit
1st Lame constant of solid skeleton	μ^S	5.583×10^6	$\mathrm{N/m^2}$
2nd Lame constant of solid skeleton	λ^S	8.375×10^6	$\mathrm{N/m^2}$
Effective density of dense solid	ρ^{SR}	2000	$\mathrm{kg/m^3}$
Effective density of pore fluid	ρ^{FR}	1000	$\mathrm{kg/m^3}$
Initial volume fraction of solid	$n^S = n^S_{0S}$	0.67	–
Darcy permeability	k^F	10^{-2}, 10^{-5}	m/s

The objective of this simple benchmark problem is to principally compare our monolithic **uv**p(3)-TR-Q2/P1 approach with existing (semi-)analytical solutions for the solid displacement and the pore-fluid pressure of an infinite half-space under dynamic loading obtained via Laplace transform [2]. It also serves to compare the accuracy of our **uv**p(3)-TR-Q2/P1 approach with the classical ones. In particular, two scenarios are tested: (1) a high permeability case with $k^F = 10^{-2}$ m/s and (2) a moderately low permeability case with $k^F = 10^{-5}$ m/s, which is the lowest permeability for which the (semi-)analytical solution could be achieved using Maple. Since the optimal time step in our method seems to be mesh independent, our computations are performed on anisotropic meshes that get finer when approaching the top (perfect drainage) boundary since at the top we have $\mathbf{t}^F = \mathbf{0}$, which must be compensated by an immediate pressure increase in a small layer below the boundary as stated in [13]. From Figure 4, we note that for each refinement level the optimal time step remains the same (nearly 5×10^{-3} s) which indicates that the optimal time step in our **uv**p(3)-TR-Q2/P1 method is indeed mesh size independent.

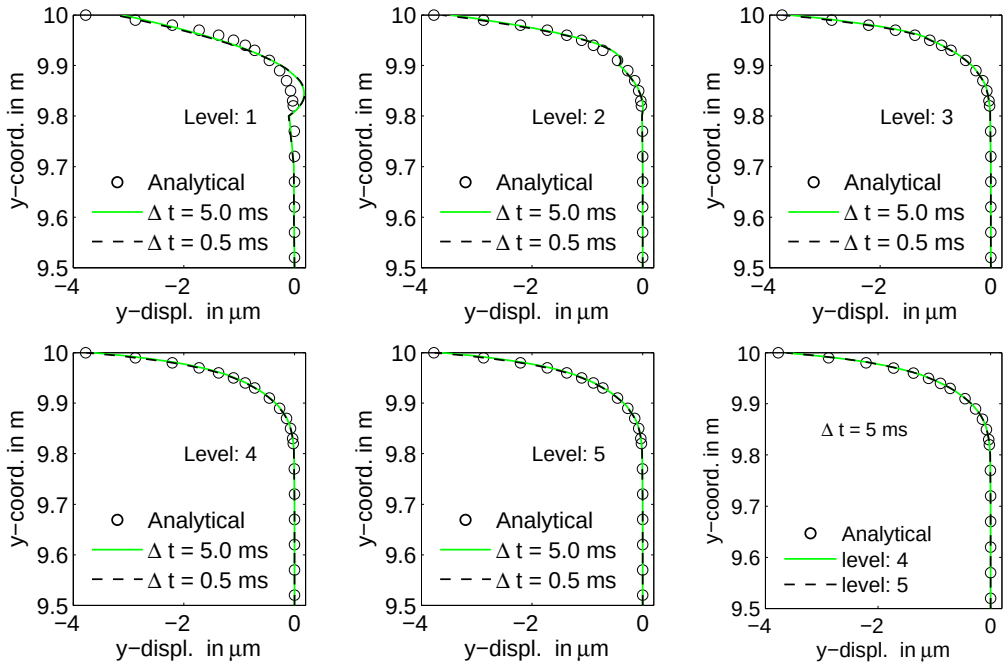

Fig. 4 Solid displacement distribution in the first half meter under the loaded top of the column using **uv**p(3)-TR-Q1/P1 for $k^F = 10^{-5} m/s$ and the rectilinear mesh (cf. Figure 3 center-right).

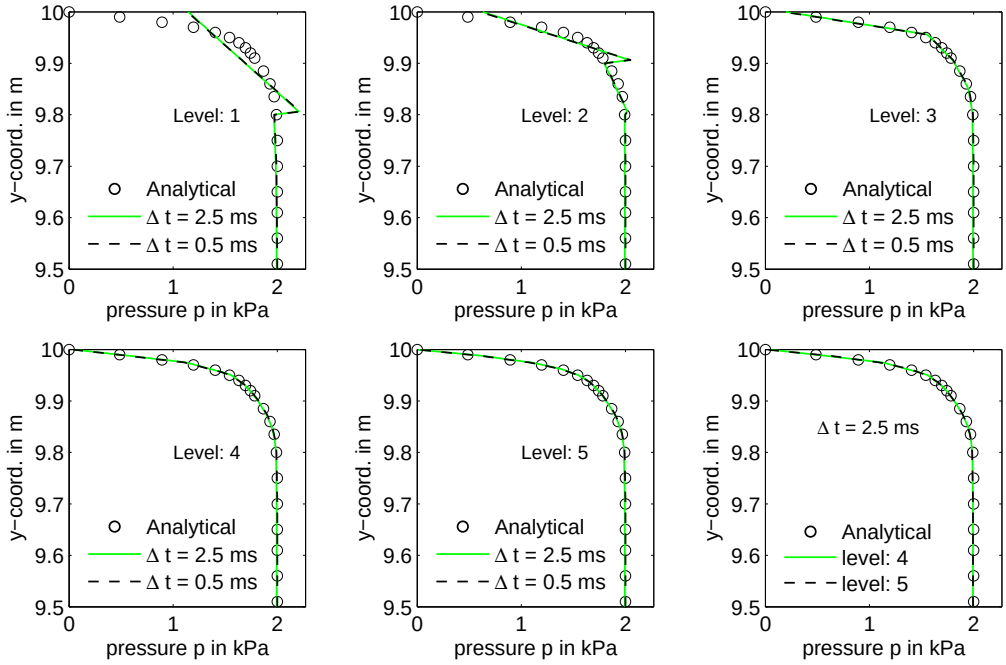

Fig. 5 Pressure distribution in the first half meter under the loaded top of the column using **uv**$p(3)$-TR-Q1/P1 for $k^F = 10^{-5}$m/s and the rectilinear mesh (cf. Figure 3 center-right).

We notice that the displacement obtains full convergence at a mesh level and time step size where the pressure is still not fully converged (see Figure 5 and 4), which indicates that a small error in the pressure does not influence the full convergence in the displacement. Moreover, from Figures 6 and 7 one can notice that for smaller k^F more elements are required to reach full convergence to capture the large gradient in the pressure. However, in both cases the optimal time step does not change. This indicates that the stability of our method is also not influenced by the value of the permeability parameter k^F.

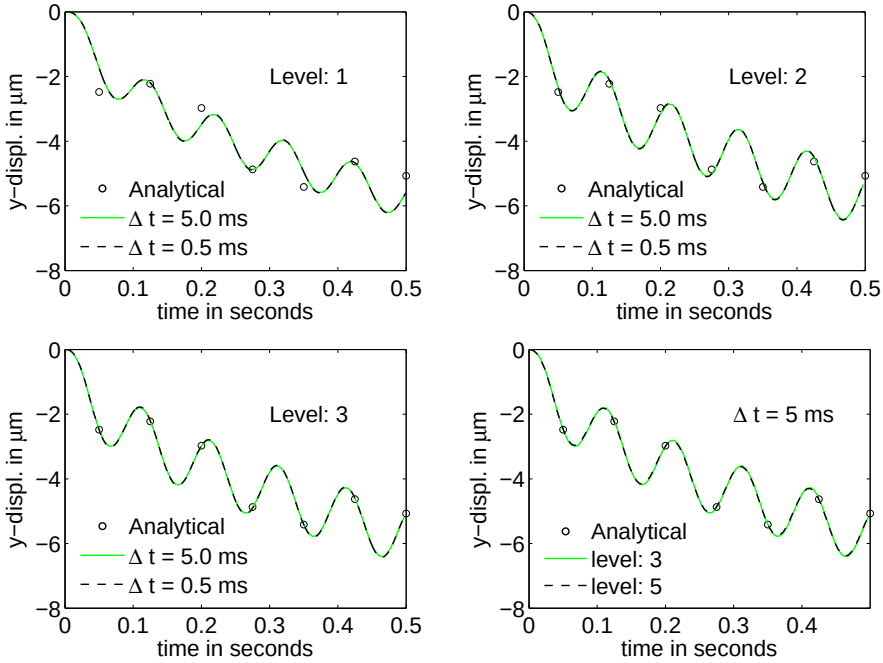

Fig. 6 y-displacement at point (1,10) vs. time using **uv**$p(3)$-TR-Q1/P1 for $k^F = 10^{-5}$m/s and rectilinear mesh (cf. Figure 3 center-right).

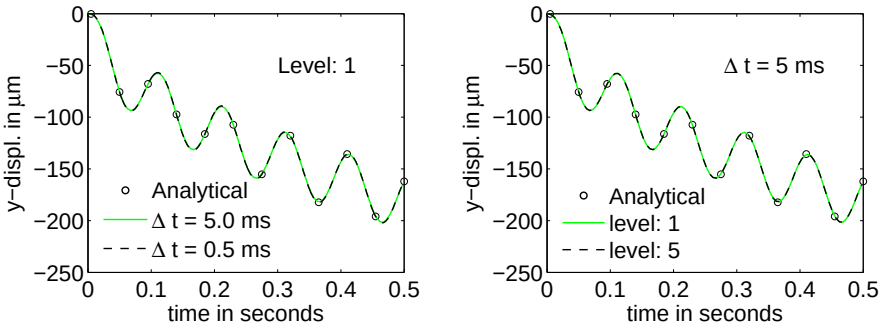

Fig. 7 y-displacement at point (1,10) vs. time using **uv**$p(3)$-TR-Q1/P1 for $k^F = 10^{-2}$m/s and rectilinear mesh (cf. Figure 3 center-right).

For comparing the accuracy of the **uv**$p(3)$-TR-Q2/P1 method with the well-established classical methods, we adopt the isotropic cartesian mesh of Figure 3. Although this kind of mesh requires a larger number of elements, it was opted because the results of the classical methods reported in [13] are based on this discretization. From Figure 8, we notice that the proposed **uv**$p(3)$-TR-Q2/P1 method provides highly accurate solutions at all selected heights of this problem except at the fully drained top boundary where we notice a small error due to the sudden pressure increase in a small layer below the surface. However, this small error can be eliminated by simply reducing the height of the elements directly under the top boundary which in turn will lead to drastic reductions in the errors at the other heights, too. In comparison to **uv**$p(2)$-TB2-QQ and **uv**$p(2)$-TB2-LL which may suffer from pressure instabilities for low permeabilities, the pressure solutions produced by **uv**$p(3)$-TR-Q2/P1 seem to be stable.

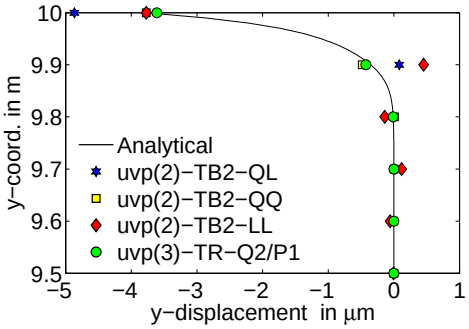

height	LL	QL	QQ	Q2/P1
9.7	0.12	0.019	0.0054	0.00027
9.8	0.13	0.0062	0.0193	0.0015
9.9	4.9	0.44	0.13	0.076
10	0	8.6	0.0001	0.16

Fig. 8 Solid displacement (left) and absolute errors in μm (right) for the first half meter below the top surface for the isotropic cartesian mesh (cf. Figure 3) and mesh level 3 (10 elem/m) and time step $\Delta t = 10^{-3}$ s.

3.1 Two-dimensional wave propagation

In this second example, we study the 2D dynamical wave propagation in a rectangular symmetric domain under plane-strain conditions (Figure 9) as presented in [3]. The material parameters are the same as before (Table 2) and the 'earthquake event' is represented by the applied distributed impulse force

$$f(t) = 10^5 \, \sin(25\,\pi\,t)\,[1 - H(t-\tau)] \quad [\mathrm{N/m^2}] \tag{29}$$

with $H(t-\tau)$ being the Heaviside step function and $\tau = 0.04\,\mathrm{s}$. The water saturated mixture domain is surrounded by impermeable, frictionless ($t_x^F = 0$ for the bottom and $t_y^F = 0$ for the left and right sides) but rigid boundaries except for the loaded top side, which is perfectly drained ($\mathbf{t}^F = \mathbf{0}$).

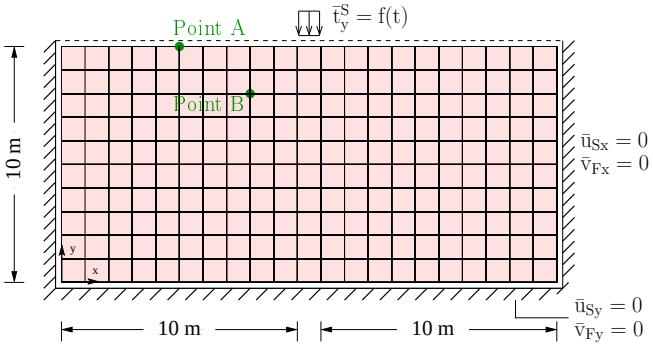

Mesh Level	#Elements (width-height)	#Unknowns
1	21-10	6 048
2	42-20	23 430
3	84-40	92 214

Fig. 9 Left: Geometry, boundary conditions and mesh level 1 of the symmetric 2D wave propagation problem. **Right**: Total number of elements and unknowns for the **uv**p(3)-TR-Q2/P1 approach.

The objective of this benchmark problem is to compare quantitatively the accuracy of our proposed monolithic **uv**p(3)-TR-Q2/P1 approach with **uv**p(2)-TB2-QL of Markert et al [13], which is known as well-accepted combination for solving such coupled problems. Here, we focus on the displacement solution at the free surface (point A) and the pressure history in the domain (point B) in the high permeability case $k^F = 10^{-2}$ m/s. In addition, since no analytical solution is available, we validate our results by comparing with [13]. From Figure 10, we can see that the optimal time step and the optimal mesh level is approx. 10^{-3} s and level 2, respectively.

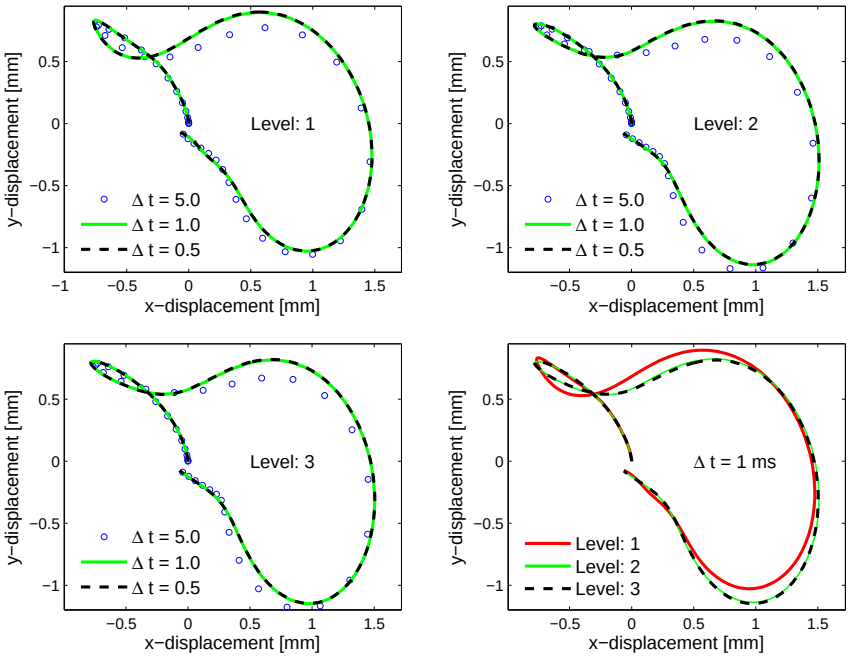

Fig. 10 Ground rolling during the 'earthquake event' at point A using **uv**p(3)-TR-Q2/P1 for $k^F = 10^{-2}$m/s for $t \in [0\ 0.2]$ s. (Δt in ms)

The direct comparison of the appropriate parameters (mesh level and time step) illustrates the perfect matching as depicted in Figure 11. Note that **uv**p(2)-TB2-QL obtains the full convergence at level 3 as indicated in Figure 11 of [13] while our **uv**p(3)-TR-Q2/P1 converges already at mesh level 2 as shown in Figure 10. The subsequent contour plots (Figure 12) generated by our approach in FEATFLOW are very similar to those in [13].

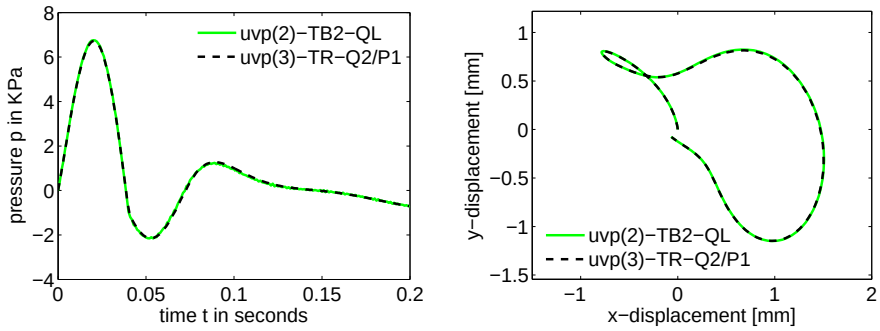

Fig. 11 Pressure history at point B and displacement history at point A using **uv**p(3)-TR-Q2/P1 for $k^F = 10^{-2}$ m/s, $\Delta t = 10^{-3}$ s and mesh level 2.

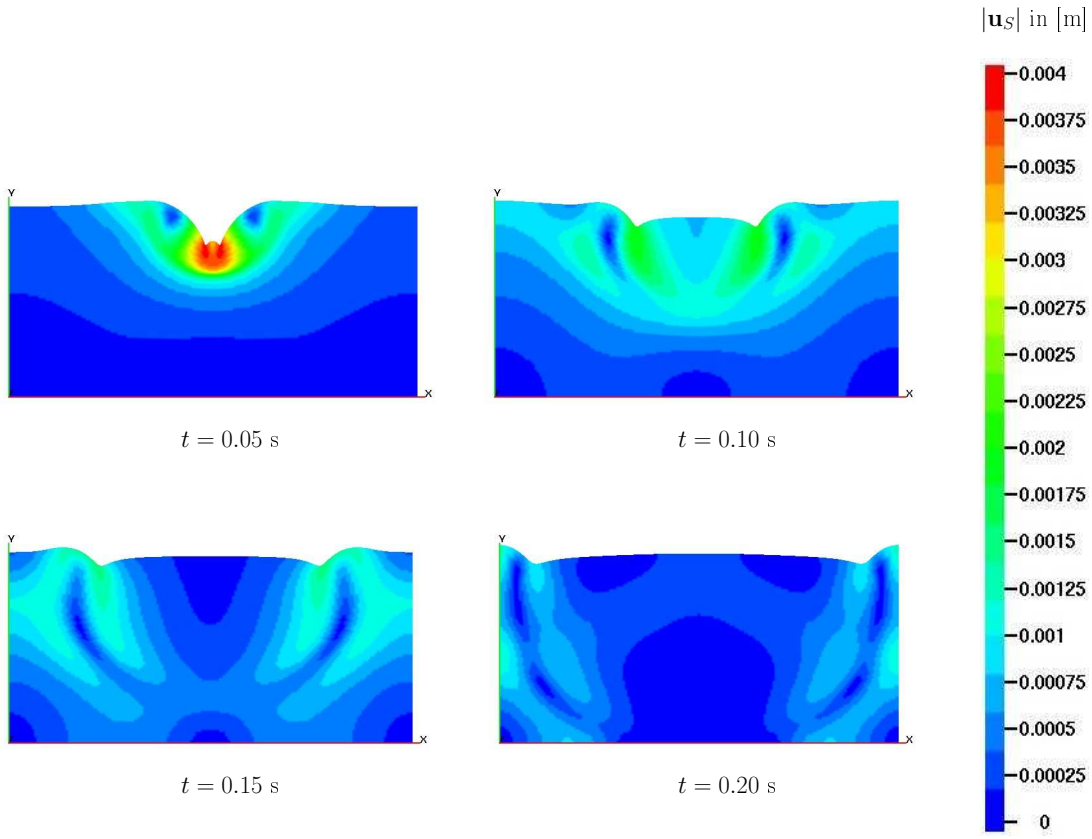

Fig. 12 Time sequence of displacement contour plots for $|\mathbf{u}_S| = \sqrt{u_{Sx}^2 + u_{Sy}^2}$ on the deformed geometry (with scaling factor 500) using uvp(3)-TR-Q2/P1, mesh level 4 and time step size 5×10^{-4} s.

4 Fast Multigrid solvers

During each time step, most of the elapsed CPU time is consumed by solving the corresponding linear systems in (28). Typically, by accuracy reasons, the arising block systems are too large to be handled by direct solvers, such that iterative schemes have to be preferred. However, due to the nature of the involved partial differential equations, the condition numbers of the arising matrices typically scale with the problem size and are quite large, such that standard single-grid schemes, for instance Krylov-space

methods like BICGSTAB or GMRES (cf. [14, 19]), are too slow. Moreover, due to the elliptic character of the incompressibility constraint, the choice of small time steps does not help since the condition numbers do not scale with the time step size.

Table 3 Averaged number of iterations per time step for preconditioned BICGSTAB in combination with **uv**p(3)-TR-Q2/P1 scheme for $k^F = 10^{-2}$ m/s until $T = 0.5$ s. See Figure 13 for the meshes and Figure 3 for the configuration.

mesh level	Cartesian		rectilinear		unstructured	
	Δt = 5	Δt = 0.5	Δt = 5	Δt = 0.5	Δt = 5	Δt = 0.5
1	10	11	10	8	11	11
2	16	17	19	9	20	11
3	29	17	37	11	40	13
4	53	16	77	15	79	17
5	95	21	151	24	141	24

Table 4 Total number of elements and unknowns (the five primary unknowns: u_{Sx}, u_{Sy}, v_{Fx}, v_{Fy} and p plus the two secondary unknowns: v_{Sx} and v_{Sy}) for **uv**p(3)-TR-Q2/P1 approach. This table is related to Figure 13.

mesh level	cartesian		rectilinear		unstructured	
	#Elements	#Unknowns	#Elements	#Unknowns	#Elements	#Unknowns
1	20	690	18	624	32	1038
2	80	2454	72	2214	128	3798
3	320	9222	288	8310	512	14502
4	1280	35718	1152	32166	2048	56646
5	5120	140550	4608	126534	8192	223878

Therefore, an excellent alternative is to solve (28) via geometrical multigrid solvers (see [15, 16, 20]), which require a hierarchy of refined mesh levels and corresponding intergrid transfer operators which are selected w.r.t. the chosen FEM spaces. What is special for the described saddle-point problems in (28) is the choice of the so-called 'smoothing operator', which in our case can be traced back to the early work by Vanka [18]. The corresponding (basic) iterative schemes can be interpreted as block Gauß-Seidel methods applied to mixed formulations of saddle-point problems. These techniques are very prominent in the CFD community to solve incompressible, resp., weakly compressible flow problems, which are based on the (generalized) Navier-Stokes equations. They have been adapted to a wide class of fluidic problems including multiphase flow, fluid-structure interaction, particulate flow, multi-component fluids, flow with chemical reactions, etc.

In the following, we perform multigrid iterations of F-cycle type, applying a fixed number of pre- and postsmoothing steps for the 3 types of grids as shown in Figure 13. The results in the subsequent Tables (5)-(8) demonstrate the very efficient convergence behaviour for several parameter configurations and they illustrate the typical convergence behaviour of multigrid solvers, namely to be more or less independent of the mesh size and the time step.

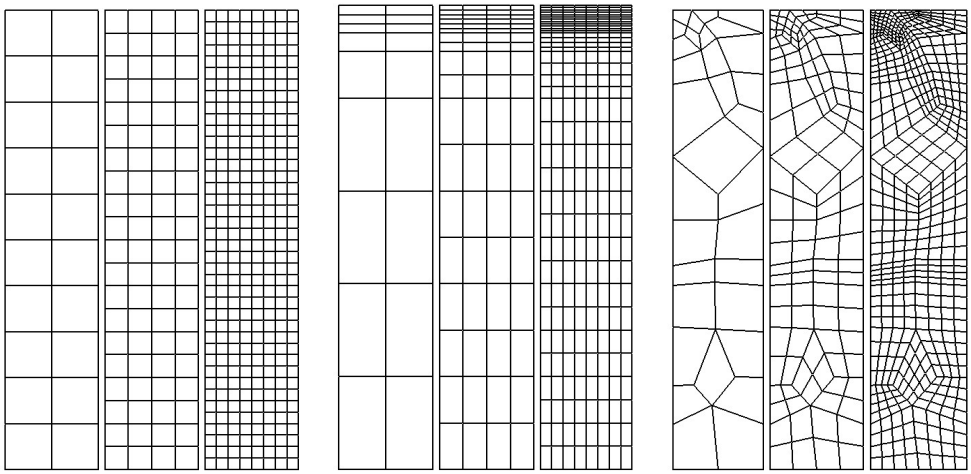

Fig. 13 Mesh level 1, level 2 and level 3 for three kinds of grids: (a) Cartesian, (b) rectilinear and (c) unstructured.

Table 5 Averaged number of iterations per time step for MG (F-4-4) for **uv**p(3)-TR-Q2/P1 for $\mathbf{k^F = 10^{-2}}$. t $\in$ [0 0.5] seconds and Δt is in ms (10^{-3} seconds).

mesh level	cartesian		rectilinear		unstructured	
	Δt = 5	Δt = 0.5	Δt = 5	Δt = 0.5	Δt = 5	Δt = 0.5
3	5.00	3.990	12.26	7.546	8.73	5.712
4	5.00	3.981	15.07	6.945	13.15	5.987
5	5.96	3.982	15.47	7.711	16.29	6.788

Table 6 Averaged number of iterations per time step for MG (F-4-4) for **uv**p(3)-TR-Q2/P1 for $\mathbf{k^F = 10^{-5}}$. t $\in$ [0 0.5] seconds and Δt is in ms (10^{-3} seconds).

mesh level	cartesian		rectilinear		unstructured	
	Δt = 5	Δt = 0.5	Δt = 5	Δt = 0.5	Δt = 5	Δt = 0.5
3	4.81	3.819	13.11	3.919	8.49	3.872
4	4.91	3.409	16.42	3.893	13.43	3.675
5	5.41	2.965	16.67	4.879	16.84	5.075

Table 7 Averaged number of iterations per time step for MG (F-8-8) for **uv**p(3)-TR-Q2/P1 for $\mathbf{k^F = 10^{-2}}$. t $\in$ [0 0.5] seconds and Δt is in ms (10^{-3} seconds).

mesh level	cartesian		rectilinear		unstructured	
	Δt = 5	Δt = 0.5	Δt = 5	Δt = 0.5	Δt = 5	Δt = 0.5
3	4.00	2.994	7.86	4.868	5.82	3.826
4	4.00	2.985	8.45	4.594	7.83	3.984
5	4.00	2.984	8.60	4.971	9.39	4.783
6	4.00	2.986	8.59	5.484	10.20	5.819

Table 8 Averaged number of iterations per time step for MG (F-8-8) for **uv**p(3)-TR-Q2/P1 for $\mathbf{k^F = 10^{-5}}$. t ∈ [0 0.5] seconds and Δt is in ms (10^{-3} seconds).

mesh level	cartesian		rectilinear		unstructured	
	Δt = 5	Δt = 0.5	Δt = 5	Δt = 0.5	Δt = 5	Δt = 0.5
3	3.81	2.886	7.31	2.920	4.88	2.910
4	3.91	2.786	9.00	2.919	7.86	2.795
5	4.70	2.721	9.18	2.999	9.81	2.998
6	4.69	2.567	8.78	4.747	10.42	5.016

5 Large-scale problems

The advantages of the described CFD techniques (special **uv**p-weak formulation, special finite element pair, fully implicit time integrator and efficient multigrid methods) become more prominent for porous media applications when working on large-scale problems such as studying the dynamic wave propagation in infinite saturated half spaces. As an example, we adopt the problem of wave propagation in an elastic structure-soil system presented in Section 4.2 of [21]. The problem is illustrated in Figure 14. Such soil-structure interaction problems have been intensively studied in the literature, cf. [9–11].

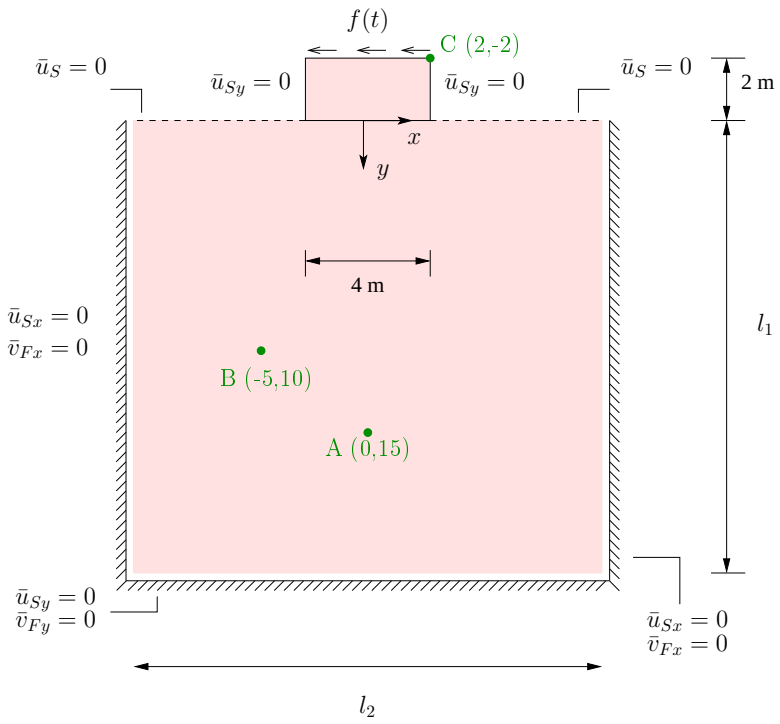

Fig. 14 Geometry of the 2D block soil problem with prescribed boundary conditions.

In the current problem, the upper block ($4 \times 2\,\mathrm{m}^2$) is considered to be in a welded contact with the soil beneath and discretized with the same type of finite elements as the soil. The applied shear impulse force is given by

$$f(t) = 10^4\,[1 - \cos(20\,\pi\,t)]\,[1 - H(t-\tau)] \quad [\mathrm{N/m^2}] \tag{30}$$

with $H(t-\tau)$ being the Heaviside step function and $\tau = 0.1\,\mathrm{s}$. The material parameters of the block and the soil are the same (cf. Table 2) with $k^F = 10^{-2}\,\mathrm{m/s}$. The unbounded domain beneath the block is replaced by a finite domain with artificial, impermeable, frictionless but rigid boundaries except for the top side which is fully drained ($\mathbf{t}^F = \mathbf{0}$).

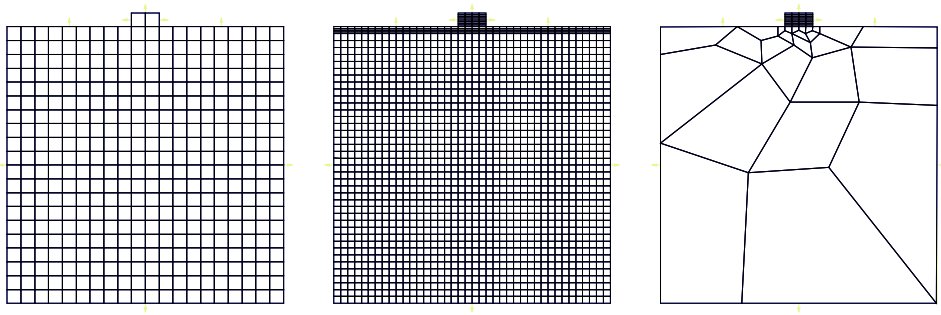

Fig. 15 Level 1 of the cartesian (left), rectilinear (middle) and unstructured grid (right) for the problem in Figure 14. For higher mesh levels, see Table 10 and Table 9.

Since the acoustic waves in the case of an unbounded domain propagate towards infinity, the vibration of, for example, point C is supposed to progress without being later disturbed by the arrival of the reflected waves resulting from using artificially fixed boundaries. To resolve this issue, the arrival of these 'undesired' waves is delayed by choosing the area ($= l_1 \times l_2$) of the represented finite domain to be large enough so that for a desired period of time, point C will vibrate before the unwanted waves travel back and corrupt the solution. Taking the area ($84 \times 81\,\mathrm{m}^2$) as reference, we notice from Figure 16 that the correct description of the horizontal displacement of point C with time is attained by adopting a finite domain of area $20 \times 20\,\mathrm{m}^2$ and $40 \times 40\,\mathrm{m}^2$ for the time intervals $t \in [0\ 0.7]\,\mathrm{s}$ and $t \in [0\ 1.4]\,\mathrm{s}$, respectively.

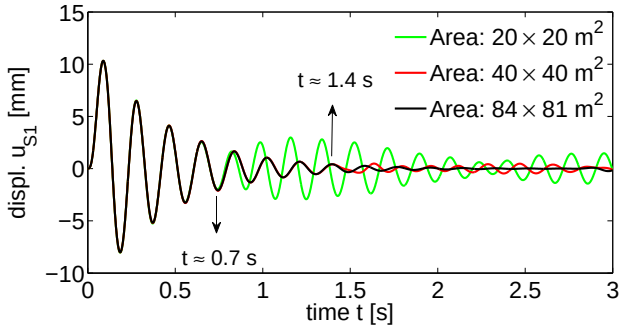

Fig. 16 Time history of the horizontal displacement at point C using **uv**p(3)-TR-Q2/P1 scheme for level 1 and the rectilinear mesh of Figure 15.

For the purpose of comparison with [21], the finite domain size is set to $40 \times 40\,\mathrm{m}^2$ and the time period is set to $t \in [0\ 1.0]\,\mathrm{s}$. Using such an equidistant (cartesian) mesh, as done in [21], requires an unnecessarily large number of finite elements, leading to correspondingly large computational costs. The results for different mesh levels are illustrated in Figure 17.

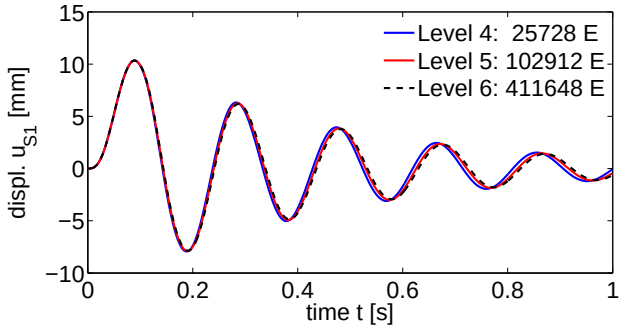

Fig. 17 Time history of the horizontal displacement at point C using **uv**p(3)-TR-Q2/P1 for the cartesian grid with optimal time step $\Delta t = 2\,\text{ms}$.

As a remark, with our **uv**p(3)-TR-Q2/P1 approach with the described multigrid solver, the results for level 3 are available in about 2 hours using a standard PC as shown in Table 9.

Table 9 Averaged number of iterations per time step for the described multigrid solver for **uv**p(3)-TR-Q2/P1 for $k^F = 10^{-2}$ m/s, $t \in [0\ 1.0]$ s and $\Delta t = 2$ ms for the cartesian grid case.

mesh level	no. elements	no. DOFs	average no. iter.	average CPU time
2 : (1 elem/m)	1608	44 406	1.964	2.5 s
3 : (2 elem/m)	6432	175 638	2.902	19 s
4 : (4 elem/m)	25 728	698 598	2.936	89 s
5 : (8 elem/m)	102 912	2 786 502	2.956	353 s
6 : (16 elem/m)	411 648	11 130 246	2.960	1446 s

However, the cartesian mesh is not the most economical way for discretizing the domain. Since our fully implicit **uv**p(3)-TR-Q2/P1 FEM approach is also suitable for unstructured meshes (see Figure 15) that can better handle the far-field artificial boundary conditions with mesh-size independent time steps (here: $\Delta t = 2\,\text{ms}$), it provides an excellent and practical alternative to structured methods (cf. [21]). Thus, even large-scale problems can be solved in reasonable time (see Table 10 and Figure 18) in combination with locally adapted, unstructured meshes.

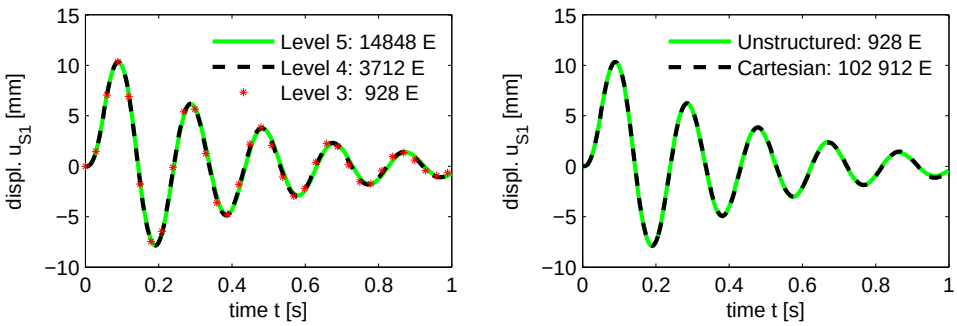

Fig. 18 Time history of horizontal displacement at point C using the **uv**p(3)-TR-Q2/P1 scheme for the unstructured grid (left) and both the cartesian and unstructured grids (right) with optimal time step $\Delta t = 2$.

Table 10 Averaged number of iterations per time step for the multigrid solver in combination with **uv**p(3)-TR-Q2/P1 for $k^F = 10^{-2}$ m/s and $\Delta t = 2$ ms for the unstructured mesh.

mesh level	no. elements	no. unknowns	average no. iter.	average CPU time
3	928	25878	-	1.45 s
4	3712	101862	3.0	10.5 s
5	14884	404166	3.0	59 s

6 Outlook

Although a dimensional analysis indicates that in a macroscopic porous media approach the following assumption might hold, namely $\operatorname{div} \mathbf{T}_E^F \ll \hat{\mathbf{p}}_E^F$ (cf. [6, 12]), such that in most cases the approximation $\mathbf{T}^F \approx -n^F p\, \mathbf{I}$ is used, we consider in our approach the fluid friction forces, too. They do not only play an important role in the (numerical) stability due to the corresponding boundary conditions, but additionally the physical consequences onto the solution are not yet clear which will be part of forthcoming simulations after having validated the described new approach. Moreover, we will also add the red-colored convective term in (16) for the purpose of comparison and analysis of the resulting physical effects which will be based on the experience from (nonlinear) CFD simulations.

Summarizing our described and forthcoming activities, it is planned to extend the models and the numerical simulations with regard to:

- the already mentioned nonlinear convective term of equation (16).
- the numerical analysis of the fluid viscosity.
- in case of non-small deformations that occur in some applications (hyper-elasticity, large strain plasticity), the corresponding volume fractions (n^S and n^F) may not be well approximated by constant values $n^F = 1 - n^S = \frac{n_0^S}{J_S}$ so that, as a consequence, the Darcy parameter is not more constant and given by the relation $k^F = k_0^F (\frac{n^F}{n_0^S})^\kappa$.
- the material nonlinearity which requires update of the stiffness matrix at every Newton iteration step which will be used to treat the nonlinear problems (cf. [4]). It is worth mentioning that if the deformation is small (like in the case of small-strain elasto- or visco-plasticity), then n^S , n^F and k^F may be approximated by constant values so that only the material stiffness matrix has to be updated.

Let us also mention that the non-linear hyperelastic model from [8] shall be implemented into FEATFLOW. In this model, the Cauchy stress tensor T_E^S is given by the relation:

$$\mathbf{T}_E^S = \frac{\mu^S}{J_S}\left(\mathbf{F}_S\mathbf{F}_S^T - \mathbf{I}\right) + \lambda^S\left(1 - n_0^S\right)\left(\frac{1}{1-n_0^S} - \frac{1}{J_S - n_0^S}\right)\mathbf{I} \tag{31}$$

Finally, the role of the absorbing boundary conditions in the unbounded domain of saturated porous media shall be implemented into our uvp(3)-TR-Q2/P1 code and directly compared with [21].

7 Conclusion

In this paper, special numerical CFD techniques which had been developed for the efficient simulation of incompressible flow problems have been extended and applied to the set of PDEs governing a saturated dynamic TPM model with intrinsically coupled solid and fluid constituents. The described model includes the solid and fluid momentum balances as well as the mixture volume balance plus the solid velocity-displacement relation. This set of PDEs has been treated by a special variational form characterized by the absence of derivatives operating on the pressure functions, and the considered fluid viscosity leads to a reduced form of boundary conditions imposed independently.

The spatial discretization has been carried out by the well-known (non-parametric) Q2/P1 finite element pair, which belongs to the best FEM choices for incompressible flow problems in terms of efficiency, accuracy and robustness, while the discretization in time has been carried out by the standard $\theta-$ scheme

($\theta = 1/2$) which leads to a fully implicit, monolithic treatment of all variables involved. For the solution of the resulting (linear) systems of equations in each time step, a fast geometrical multigrid solver with special block Vanka smoother has been realized which leads to convergence rates being independent of time step and mesh size, which is important particularly for large scale problems. For validation purposes, canonical one and two-dimensional wave propagation examples from the literature were opted to validate and to compare the new approach with classical ones.

As a conclusion, based on the comprehensive investigation of several test cases and in comparison with the results of [13], we recommend the fully implicit approach using our uvp(3)-TR-Q2/P1 method in combination with the described special multigrid components which demonstrate excellent numerical results regarding accuracy and robustness, particularly regarding quantitative comparisons with the classical techniques as described in [13]. Additionally, we provide an outlook to the next steps, particularly w.r.t. adding more realistic (nonlinear) model components into our simulation framework.

Acknowledgements We thank Michael Köster for the intensive support in the stage of implementations into FEATFLOW. Moreover, this work was partially support by the DFG grant TU102/34-1.

References

1. de Boer R, Ehlers W (1990) The development of the concept of effective stresses. Acta Mech 83:77–92
2. de Boer R, Ehlers W, Liu Z (1993) One-dimensional wave propagation in fluid saturated incompressible porous media. Arch Appl Mech 63:59–72
3. Breuer S (1999) Quasi-static and dynamic behavior of saturated porous media with incompressible constituents. Transp Porous Media 34:285–303
4. Damanik H, Hron J, Ouazzi A, Turek S (2009) A monolithic FEM–multigrid solver for non–isothermal incompressible flow on general meshes. Journal of Computational Physics 228:3869–3881
5. Diebels S, Ehlers W (1996) Dynamic analysis of a fully saturated porous medium accounting for geometrical and material non-linearities. Int J Numer Methods Eng 39:81–97
6. Diebels S, Ehlers W, Markert B (2001) Neglect of the fluid extra stresses in volumetrically coupled solid-fluid problems. ZAMM 81:521 – 522
7. Ehlers W (2002) Foundations of multiphasic and porous materials. In: Ehlers W, Bluhm J (eds) Porous Media: Theory, Experiments and Numerical Applications, Springer-Verlag, Berlin, pp 3–86
8. Eipper G (1998) Theorie und Numerik finiter elastischer Deformationen in fluidgesättigten porösen Medien. Dissertation, Bericht Nr. II-1 aus dem Institut für Mechanik (Bauwesen), Universität Stuttgart
9. von Estorff O (1991) Dynamic response of elastic blocks by time domain BEM and FEM. Computers & Structures 38:289–300
10. von Estorff O, Firuziaan M (2000) Coupled BEM/FEM approach for nonlinear soil/structure interaction. Eng Anal Boundary Elem 24:715–725
11. Kim D, Yun C (2000) Time-domain soil-structure interaction analysis in two-dimensional medium based on analytical frequency-dependent infinite elements. Int J Numer Methods Eng 47:1241 – 1261
12. Markert B (2007) A constitutive approach to 3-d nonlinear fluid flow through finite deformable porous continua. Transp Porous Med 70:427–450
13. Markert B, Heider Y, Ehlers W (2010) Comparison of monolithic and splitting solution schemes for dynamic porous media problem. Int J Numer Meth Eng 82:1341–1383
14. Saad Y, Schultz M (1986) A generalized minimal residual method for solving nonsymmetric linear systems. SIAM J Sci Statist Comput 7:856–869
15. Strang G (2007) Computational Science and Engineering. Wellesley-Cambridge press, London
16. Turek S (1999) Efficient solvers for incompressible flow problems: An algorithmic and computational approach. Springer
17. Turek S, Hron J, Madlik M, Razzaq M, Wobker H, Acker J (2010) Numerical simulation and benchmarking of a monolithic multigrid solver for fluid–structure interaction problems with application to hemodynamics. In: Bungartz H, Mehl M, Schäfer M (eds) Fluid-Structure Interaction II: Modelling, Simulation, Optimisation, Springer, doi 10.1007/978-3-642-14206-2
18. Vanka S (1986) Block-implicit multigrid solution of navier-stokes equations in primitive variables. Journal of Computational Physics 65:138–158

19. Van der Vorst H (1992) Bi-cgstab: A fast and smoothly converging variant of bi-cg for the solution of nonsymmetric linear systems. SIAM J Sci Stat Comput 13:631–644
20. Wobker H, Turek S (2009) Numerical studies of Vanka–type smoothers in computational solid mechanics. Advances in Applied Mathematics and Mechanics 1(1):29–55
21. Y Heider BM, Ehlers W (2012) Dynamic wave propagation in infinite saturated porous media half spaces. Computational Mechanics 49:319–336